JET–P(99)46

L C Ingesson

A Tomographic Reconstruction Method with Generalized Natural Basis Functions and *a priori* Information

JET–P(99)46

A Tomographic Reconstruction Method with Generalized Natural Basis Functions and *a priori* Information

L C Ingesson.

JET Joint Undertaking, Abingdon, Oxfordshire, OX14 3EA,

Preprint of a Paper to be submitted for publication in Inverse Problems (IOP)

February 2000

ABSTRACT

Series-expansion tomography methods that use natural basis functions (NBFs), also called natural pixels, often use iterative solution techniques or solution by truncated singular value decomposition (TSVD). Here, solution by constrained optimization is proposed. It is shown that significant improvements in the tomographic reconstructions can be obtained, in particular when the coverage by the imaging system is irregular. The analogy between regular NBFs and the filtered backprojection or convolution-backprojection tomography method suggests maximum smoothness in projection space as object function (i.e. *a priori* information) in the constrained optimization. A further improvement was found by employing NBFs that correspond to a bi-linear interpolation in projection space. The new NBF method is compared with various tomography methods: constrained optimization with local basis functions, NBFs with TSVD, and an iterative projection-space reconstruction method.

PACS classification numbers: 42.30.Wb, 52.70.Kz

1. INTRODUCTION

The filtered-backprojection (FBP) method, also known as convolution-backprojection, is a good and much-used tomography method [1]. It is applicable when the imaging system has a regular coverage, for instance parallel lines of sight, and the individual measurements can be approximated by line integrals. In this paper two-dimensional tomography methods are considered that can be applied to the more general case in which the coverage of the system is irregular and the beam-widths of the measurements cannot be neglected. Methods exist that, in combination with FBP, pre-process the measurements [2–5] or post-process the tomographic reconstruction [2,5,6] to take into account the finite beam-width effects, or iteratively apply FBP and the beam-width correction [7,8]. The irregular coverage can be transformed to a regular coverage by interpolation in projection space, as has been described by Peters and Lewitt [9] and Ingesson and Pickalov [7]. The finite beam widths can also be taken into account in the latter method [10], which is referred to as the iterative projection-space reconstruction (IPR) method. Series-expansion tomography methods [1,11], in general, can cope with both the irregular coverage and finite beam widths. One particular series-expansion method that is considered in detail in this paper, is the natural basis function (NBF) method, also know as natural pixel method [12] (in this paper the term natural basis function is preferred over natural pixel because it brings out the relationship with other basis functions better).

The relationship between the backprojection operations in the NBF and FBP methods, in the case of regular coverage, has been noticed before [13–15]. The aim of this paper is to discuss this relationship and generalize it to irregular coverage by means of the generalized NBFs introduced by Hsieh *et al* [15]. With the recognition of this relationship one can apply *a priori* information as regularization in the NBF methods, whereas usually NBF methods are implemented iteratively [12] or by means of truncated singular value decomposition TSVD) [13,14]. It will

also be shown that the IPR method can be reformulated as an NBF method with somewhat different generalized NBFs than above, and be solved including *a priori* information. Both the NBF and IPR methods that include *a priori* information are shown to improve the reconstructions with respect to the conventional implementation of NBF and IPR methods. The results are also compared with a constrained-optimization (CO) method with local-basis functions (LBF) in real space.

The structure of this paper is as follows. Section 2 introduces the terminology and notation, and discusses FBP, the inclusion of imaging-system properties, LBFs, NBFs and the relationship between regular NBF methods and FBP. The implementation of CO-NBF and the IPR methods is described in section 3. Phantom simulations comparing the methods are presented in section 4 and the results are discussed in section 5. The basis functions and phantom simulations discussed are relevant for the two-dimensional tomographic reconstruction of soft x-ray emission in the JET (Joint European Torus) tokamak, a device for thermonuclear fusion research (for a detailed account of soft x-ray tomography at JET, see reference 16).

2. BACKGROUND

2.1 Description with continuous functions and line integrals

Straight-line integrals $f(p,\xi)$ of local properties $g(x,y)$ of an object, such as emission or absorption, are described by the Radon transform

$$f(p,\xi) = \Re_{x,y}\{g(x,y)\}(p,\xi) = \iint g(x,y)\,\delta(p + x\sin\xi - y\cos\xi)\,\mathrm{d}x\,\mathrm{d}y\,. \qquad (1)$$

The support of the function $g(x,y)$ is assumed to be bounded, i.e. $g(x,y)$ is zero outside a region with radius a, so that the integrals are over a finite region in the space with Cartesian coordinates (x,y). The parameters of a line (p,ξ) are coordinates of a space called projection space; p is the signed distance between the line and the origin, and ξ is the angle of the line with the positive x axis (note that some authors use a definition for the angle that is different by $\pi/2$). The inversion of equation (1), i.e. finding $g(x,y)$ from given $f(p,\xi)$, is called the tomographic inversion or tomographic reconstruction. The image of $f(p,\xi)$ is called sinogram and the reconstruction $g(x,y)$ is called tomogram. Figure 1(a) shows an example of a soft x-ray emission profile in the JET tokamak and 1(b) the corresponding sinogram. The lines of sight of the 197 detectors of the soft x-ray imaging system are also indicated in figures 1(a) and 1(b).

A numerically stable way to obtain the inverse of the Radon transform is by means of a filtering of the function $f(p,\xi)$ and then backprojection. The filtering operation is given by the convolution

$$h(p,\xi) = \int_{-\infty}^{\infty} f(p',\xi)\,\eta(p - p')\,\mathrm{d}p' \qquad (2)$$

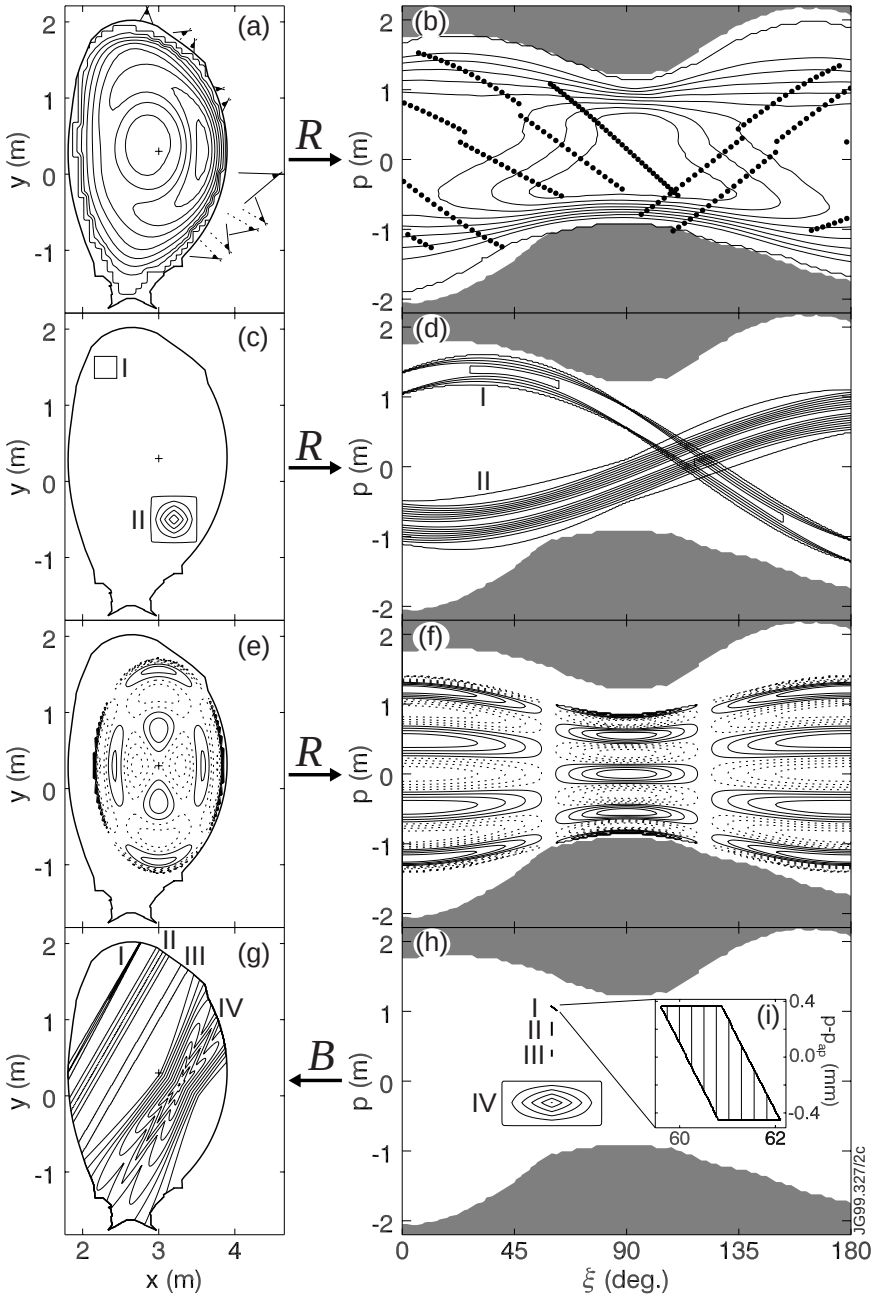

Fig.1: Illustration of various types of basis functions in xy *space (a,c,e,g) and projection space (b,d,f,h) as contour plots. (a,b) Soft x-ray emission profile used as phantom [identical to figure 3(a)] and its sinogram. The fans in (a) indicate the extent of the viewing fans of the JET soft x-ray imaging system (each with 18 channels, except the top one which has 35 channels); the average lines of sight are indicated by points in (b). (c,d) Local basis functions (exaggerated size); I: square pixel; II: "pyramid" (linear interpolation between grid points). (e,f) One Cormack global basis function (cosine component with parameters* $n = 2$, $m = 3$ *[18]). Normally the Cormack basis functions are given in polar coordinates; here these coordinates have been transformed to elliptical coordinates by a linear stretching transformation (thus keeping straight lines straight) of* (x,y) *and* (p,ξ) *in the* y *direction. (g,h) Natural basis functions; I: geometric function of one soft x-ray detector (blow up of projection-space coverage in (i), see reference 17 for details;* $p_{ap}(\xi)$ *is the* p *value that corresponds to lines through the centre of the aperture); II: triangular strip; III: constant strip; IV: IPR-like basis functions (exaggerated size). The relationship between* xy *space and projection-space quantities is indicated by the Radon and Backprojection operators. The origin for projection space is indicated by a cross in (a,c,e,g). The boundary of the reconstruction region (the first wall structures of the tokamak vacuum vessel) is given by a thick line; lines of sight passing outside the boundary are in the dark region indicated in projection space.*

where in any practical implementation $\eta(p)$ is a band-limiting filter function that is described in the standard works on this method, e.g. references [1,11]. The continuous backprojection is given by

$$\begin{aligned} g(x,y) = \mathsf{B}_{p,\xi}\{h(p,\xi)\}(x,y) &= \int_0^{\pi} h(-x\sin\xi + y\cos\xi, \xi)\,\mathrm{d}\xi \\ &= \int_0^{\pi}\int_{-\infty}^{\infty} h(p,\xi)\,\delta(p + x\sin\xi - y\cos\xi)\,\mathrm{d}p\,\mathrm{d}\xi. \end{aligned} \tag{3}$$

The order of the operations has given rise to the names filtered backprojection and convolution backprojection for this method. In the numerical implementation for discrete measurements equations (2) and (3) have to be discretized.

2.2. Inclusion of imaging-system properties

When the measurements cannot be approximated by line integrals, the geometric properties of the imaging system have to be taken into account. This can be done either in projection space with a geometric function $k(p,\xi \mid p',\xi')$ that blurs the pure line-integral values $f(p,\xi)$, or in xy space with a geometric function $K(p,\xi \mid x,y)$. The blurred measurements (indicated by the hat) are described by

$$\hat{f}(p,\xi) = \int_0^{\pi}\int_{-\infty}^{\infty} f(p',\xi')\; k(p,\xi \mid p',\xi')\,\mathrm{d}p'\,\mathrm{d}\xi' \tag{4}$$

or

$$\hat{f}(p,\xi) = \iint g(x,y)\; K(p,\xi \mid x,y)\;\mathrm{d}x\;\mathrm{d}y. \tag{5}$$

To indicate that a more general kernel than in equation (1) is used, equation (5) is sometimes referred to as the generalized Radon transform. It can be shown that the geometric functions in xy space and projection space are related by the backprojection operator [17]

$$K(p,\xi \mid x,y) = \mathsf{B}_{p',\xi'}\{k(p,\xi \mid p',\xi')\}(x,y).$$

The geometric functions can include three-dimensional effects of the imaging system, provided the emission does not vary in the perpendicular direction to the two-dimensional reconstruction plane [17]. A description very similar to the one in functions $K(p,\xi \mid x,y)$ and $k(p,\xi \mid p',\xi')$, including three-dimensional effects and their relationship by something similar to the backprojection operator, has been given by Verly [6]. There, however, the parametrization was given in imaging-system parameters of the transmission tomography system (position in detector and source plane), and the step to projection space was not made. In actual imaging systems discrete, rather than continuous, measurements are made. For individual detectors indicated by index i [with average line of sight (p_i,ξ_i)], that may have very different geometric

properties from each other, the geometric functions in real space and in projection space may be written as $K_i(x,y)$ and $k_i(p,\xi)$ respectively. An illustration of the functions $K_i(x,y)$ and $k_i(p,\xi)$ for one channels of the soft x-ray imaging system at JET is given in figures 1(g) and 1(i), respectively.

2.3. Series-expansion (discretization)

Consider the object $\hat{g}(x,y)$, which is an approximation of $g(x,y)$ and given by

$$\hat{g}(x,y) = \int\int g(x',y')\ B(x,y \mid x',y')\ \mathrm{d}x'\ \mathrm{d}y'. \tag{6}$$

If $B(x,y|x',y')$ is shift-invariant, i.e. $B(x,y \mid x',y') = B(x-x',y-y')$, equation (6) describes a blurring of the function $g(x,y)$. If one only has samples of $\hat{g}(x,y)$ in a number of discrete points (x_j,y_j), on a regular grid one can approximate equation (6) by a summation

$$g(x,y) \approx \hat{g}(x,y) \approx \sum_j g_j\ B(x-x_j,y-y_j)\ . \tag{7}$$

Equation (7) can be viewed as a series expansion of the function $\hat{g}(x,y)$ on a set of local basis functions (LBFs) $B_j(x,y) = B(x-x_j,y-y_j)$ (which may be orthogonal, but do not have to be) with expansion coefficients g_j. Such discretizations are employed in tomographic reconstruction methods of the series-expansion type [11]. Two examples of typical LBFs (exaggerated in size) are given in figure 1(c): in square constant pixels the expansion coefficient g_j corresponds to the average value of $g(x,y)$ over pixel j, in "pyramid" basis functions g_j corresponds to the value $g(x_j,y_j)$ and the expansion gives the bi-linearly interpolated values in any point (x,y). Substitution of equation (7) into (1) shows that

$$f(p,\xi) \approx \sum_j g_j\ b(p,\xi \mid x_j,y_j) \tag{8}$$

where $b(p,\xi \mid x',y')$is the Radon transform of $B(x,y \mid x',y')$ [see figure 1(d)]. Even if the LBFs are orthogonal in xy space, their Radon transforms are not orthogonal in projection space, which means that in solving equation (8) all basis functions interact, i.e. all expansion coefficients g_j depend on each other. Including the geometric function, i.e. substituting equation (7) into (5), gives

$$\hat{f}_i = \hat{f}(p_i,\xi_i) = \sum_j g_j K_{ij} \tag{9}$$

where the geometric matrix $\boldsymbol{K}$ is given by

$$K_{ij} = \iint K(p_i,\xi_i \mid x,y)\ B(x_j,y_j \mid x,y)\ \mathrm{d}x\ \mathrm{d}y \tag{10}$$

or alternatively by substituting equation (8) into (4)

$$K_{ij} = \iint k(p_i,\xi_i \mid p,\xi)\ b(p,\xi \mid x_j,y_j)\ \mathrm{d}p\ \mathrm{d}\xi.$$

Instead of LBFs, it is also possible to make an expansion into a set of global basis functions $B_j(x,y)$ (where the index j now numbers the parameters that distinguish the members of the set). One example of a class of global basis functions that are orthogonal and also have orthogonal Radon transform, are the Cormack basis functions [18], see figures 1(e) and 1(f). Because the basis functions in projection space are orthogonal, the g_j can all be solved independently from equation (8).

In analogy with equation (6), one can also choose basis functions that are parametrized by (p,ξ):

$$\hat{g}(x,y) = \int_0^{\pi} \int_{-\infty}^{\infty} \tilde{g}(p,\xi)\ B(x,y \mid p,\xi)\ \mathrm{d}p\ \mathrm{d}\xi. \tag{11}$$

Similarly to equation (7), discretization of equation (11) gives

$$g(x,y) \approx \hat{g}(x,y) \approx \sum\nolimits_j \tilde{g}_j\ B(x,y \mid p_j,\xi_j)\,. \tag{12}$$

Such basis functions, called natural basis functions (NBFs), are strip shaped as illustrated in figure 1(g). Comparison with equation (3) indicates that (11) can be considered to be a blurred backprojection, i.e. having a kernel of finite width. Equation (12) is therefore a discrete implementation of the backprojection operator [13–15] and the function $\tilde{g}(p,\xi)$ is an approximation of $h(p,x)$ of equation (3). This observation is further discussed in the appendix. Equation (9) is now

$$\hat{f}_i = \hat{f}(p_i,\xi_i) = \sum\nolimits_j \tilde{g}_j K_{ij}\,. \tag{13}$$

The continuous version is

$$\hat{f}(p,\xi) = \int_0^{\pi} \int_{-\infty}^{\infty} \tilde{g}(p',\xi')\ A(p,\xi \mid p',\xi')\ \mathrm{d}p'\ \mathrm{d}\xi'\,. \tag{14}$$

As equation (10), the matrix $\boldsymbol{K}$ and function $A(p,\xi \mid p',\xi')$ is given by

$$K_{ij} = A(p_i,\xi_i \mid p_j,\xi_j) \text{ and } A(p,\xi \mid p',\xi') = \iint K(p,\xi \mid x,y)\, B(x,y \mid p',\xi')\, \mathrm{d}x\ \mathrm{d}y\,. \tag{15}$$

Because equation (13) contains both the measurement operation (“projection”) and the backprojection, it is sometimes referred to as the projection-backprojection operator. In NBF methods, after solving $\tilde{g}_j$ from equation (13), the result is obtained by backprojecting with equation (12). In the literature usually NBFs that are equal to the geometric function, i.e. $B(x,y \mid p,\xi) = K(p,\xi \mid x,y)$ are used, which often are simple strips. In the present case, the functions $K_i(x,y)$ are complicated functions [see fig.1(g)] and the coverage of the system is very irregular [see fig.1(b)]; therefore it is better to choose generalized NBFs [15] such as constant strips or triangular strips [see fig.1(b)]. The name natural basis function, or natural pixel, stems from the observation that in a certain sense such basis functions are more consistent with the measurements than other types of basis functions, and therefore more “natural” [12].

2.4. Relationship between FBP and NBF methods

In the appendix it is shown that $\tilde{g}(p,\xi)$ in equation (14) is equivalent to the filtered $h(p,\xi)$ of (2), and that therefore the discrete versions $\tilde{g}_j$ [solution of equation (13)] and $h(p_j,\xi_j)$ are also equivalent. Usually no explicit use is made of *a priori* information in the solution of $\tilde{g}_j$ from equation (13) in NBF methods. Often iterative techniques or TSVD are used to find a (regularized) solution [12–14]. Because the meaning of $\tilde{g}_j$ has not been considered in those applications, no attempt has been made to include *a priori* information about $\tilde{g}_j$. The resulting tomographic reconstructions can seem noisy. In contrast, in FBP the high spatial-frequency components of the measurements are filtered out by the band-limited filter function in equation (2). After filtering, $\tilde{g}(p,\xi)$ is likely to be a smooth function. Because smoothness is routinely used as object function in constrained-optimization (CO) methods [19] for solving systems of equations, smoothness can very well be applied as *a priori* information when solving equation (13).

Suppose $\tilde{g}(p,\xi)$ can be approximated by the series expansion

$$\tilde{g}(p,\xi) \approx \sum_j \tilde{g}_j \tilde{B}(p,\xi \mid p_j,\xi_j).$$

Backprojection gives back equation (12) if the backprojection of $\tilde{B}(p,\xi \mid p_j,\xi_j)$ is identified with $B(x,y \mid p_j,\xi_j)$. Figure 1(h) shows the projection-space shape, i.e. inverse backprojections, of the NBFs of fig.1(g). Thus, the functions $\tilde{B}(p,\xi \mid p_j,\xi_j)$ are (local) basis functions in projection space to approximate $\tilde{g}(p,\xi)$. Note that these projection-space basis functions are distinct from the basis functions in figures 1(b) and 1(d), which approximate $f(p,\xi)$ by equation (8). Beam-width effects are taken into account when $\tilde{g}(p,\xi)$ is solved from $\hat{f}(p,\xi)$. In the application of FBP to systems with non-negligible beam widths, $f(p,\xi)$ has to be reconstructed from $\hat{f}(p,\xi)$ first (pre-filtering [2–5,10]), or one pretends that $\hat{f}(p,\xi)$ can be used instead of $f(p,\xi)$ and filters after the tomographic reconstruction [2,5,6].

The basis functions $\tilde{B}(p,\xi \mid p_j,\xi_j)$ that correspond to constant or triangular strips cover projection space rather poorly because they have no spread in the ξ direction. This coverage can be improved by using pyramid basis functions, which describe a bi-linear interpolation between grid points in projection space (or a higher order function, such as B-splines [20]), as shown in figure 1(h) (exaggerated size). Backprojection of this function leads to a rather complicated shape in *xy* space [figure 1(g)], which one would expect to have better properties than the other NBFs because they cover projection space more completely. Similar basis functions in projection space have been used in the IPR method [7]. Thus, the proposed tomographic reconstruction method can also be compared with the IPR methods.

The considerations in the appendix lead to obvious *a priori* information that can be used in the tomographic reconstruction and can be expected to lead to a better result than without *a priori* information. The FBP method is mainly suitable to imaging systems with regular coverage

(parallel beams or fan beams) and for which the measurements can be approximated by line integrals. Given the equivalence of FBP and NBF methods for parallel strip measurements and parallel strip basis functions, one can consider the generalized NBF method to be an important generalization of FBP that can cope with complicated geometric functions and irregular coverage. Beam-widths and irregular coverage can be taken into account in FBP by the IPR method. However, the proposed basis function that is similar to the one used in the IPR method is an elegant improvement on the IPR method, because, instead of iteratively making the solution self-consistent, the NBF method with this basis function can find a consistent solution in one step.

3. IMPLEMENTATION OF CONSTRAINED-OPTIMIZATION NBF METHOD AND IPR METHOD

The phantom used in this paper [figs.1(a) and 3(a)] is a typical soft x-ray emission profile in JET. The sinogram of this phantom, after filtering by the FBP filter (with a Shepp-Logan filter) as give by equation (2), is shown in fig.2(a). The filtered sinogram is fairly smooth and, as indicated in section 2.4, an object function describing smoothness could be applied in a CO method for the solution of equation (13). The unsmoothness of the function $\tilde{g}(p,\xi)$ can be quantified by the scalar

$$< \tilde{\boldsymbol{g}} \mid \boldsymbol{\Omega} \mid \tilde{\boldsymbol{g}} >= \int_0^{\pi} \int_{-\infty}^{\infty} \left[c_0(p,\xi)\tilde{g}^2(p,\xi) + c_p(p,\xi)\left(\frac{\partial^2 \tilde{g}}{\partial p^2}\right)^2 + c_\xi(p,\xi)\left(\frac{\partial^2 \tilde{g}}{\partial \xi^2}\right)^2 \right] \mathrm{d}p\,\mathrm{d}\xi \qquad (16)$$

where the Dirac notation is used for the inner product. Periodicity of projection space requires that the values at (p,π) are equal to those at $(-p,0)$. The unsmoothness can be minimized with a constraint by the Lagrange multiplier method. As constraint the discrepancy condition [21] is used, i.e.

$$< \boldsymbol{K}\tilde{\boldsymbol{g}} - \hat{\boldsymbol{f}} \mid \boldsymbol{K}\tilde{\boldsymbol{g}} - \hat{\boldsymbol{f}} > \leq < \boldsymbol{\varepsilon} \mid \boldsymbol{\varepsilon} > \qquad (17)$$

where ε is the estimated measurement error. Because the object function (16) is quadratic, the CO can be achieved by solving the matrix equation

$$(\lambda \boldsymbol{K}^{\mathsf{T}}\boldsymbol{K} + \boldsymbol{\Omega})\tilde{\boldsymbol{g}} = \lambda \boldsymbol{K}^{\mathsf{T}}\hat{\boldsymbol{f}}\,. \qquad (18)$$

The Lagrange multiplier λ can be found by either iteratively solving equation (18) for varying λ until the constraint (17) is satisfied, or noniteratively [19].

The parameters c_0, c_p and c_ξ in equation (16), which can be either constant or vary as a function of p and ξ, are free and have to be chosen appropriately as they influence the result. The parameter c_0 is, strictly speaking, not relevant for smoothness: it puts a penalty on non-zero values. Often c_0 is set to a large value in regions where the object [$\tilde{g}(p,\xi)$ in this case] is expected to be small, for example on the edge. As figure 2(a) shows this is not appropriate for

$\tilde{g}(p,\xi)$ which does not go to zero on the edge of the reconstruction region (it depends on whether one knows beforehand exactly the region where $\tilde{g}(p,\xi)$ is non-zero). Therefore, $c_0(p,\xi)=0$ was chosen everywhere. The ratio of c_p and c_ξ determines the anisotropy in smoothness between the p and ξ directions. Figure 2(a) shows that $\tilde{g}(p,\xi)$ has more variation in the p direction than in the ξ direction. It was found that the ratio of c_p and c_ξ was not a very sensitive parameter; a ratio of $(c_\xi/\pi)/(c_p/a)=10-20$ gave adequate results.

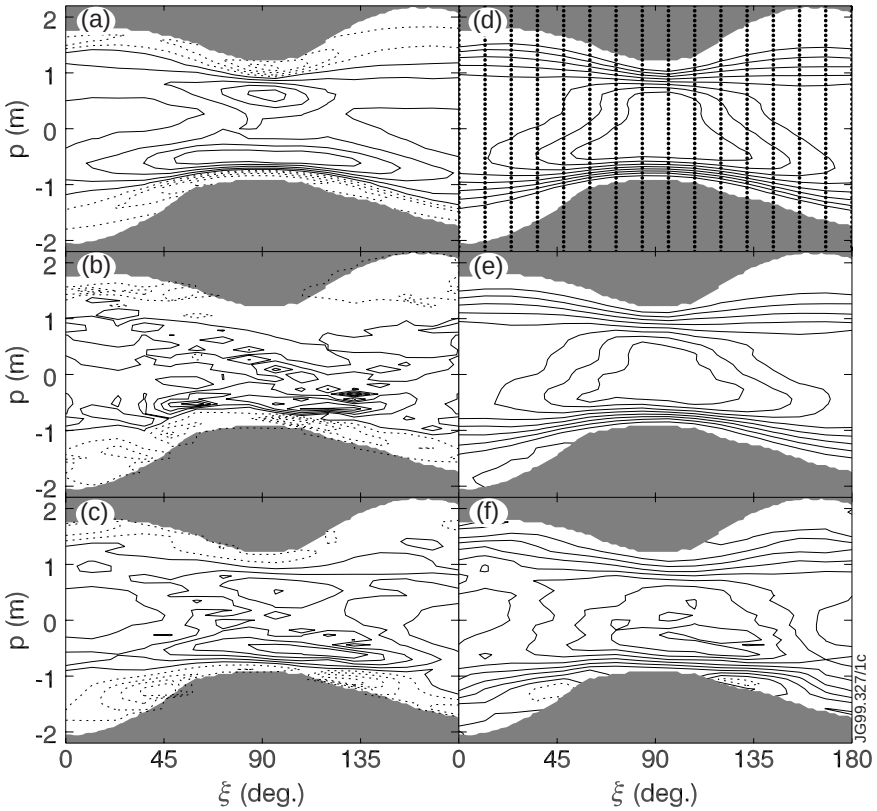

Fig.2: Filtered sinograms and sinograms obtained by various methods. (a) h(p,ξ)*, i.e. sinogram of figure 1(a) filtered with a band-limited FBP filter (Shepp-Logan) by equation (2). (b)* $\tilde{g}(p,\xi)$ *obtained by inversion of equation (13) by means of TSVD, method B. (c)* $\tilde{g}(p,\xi)$ *obtained by inversion of equation (13) by means of CO-NBF, method E. (d) Sinogram* f(p,ξ) *of phantom, i.e. equal to figure 1(b), with grid points indicated. (e) Sinogram* f(p,ξ) *reconstructed by IPR method, method C. (f) Sinogram* f(p,ξ) *calculated by applying equation (22), using equation (21) for line-integral basis and geometric functions, to* $\tilde{g}(p,\xi)$ *reconstructed by the CO-NBF, method E. The contour levels in (b), (c) and (f) are not to the same scale of the other corresponding figures. The dark region has the same meaning as in fig.1. Dotted contours indicate negative values.*

The results of the CO-NBF method is compared with, among other methods, the IPR method. An improved version of the IPR method was used. In the original IPR method [7] the sinogram values, expanded on pyramid basis functions in projection space, are reconstructed iteratively from the measurements. The consistency of the sinogram is ensured mainly by Gerchberg-Papoulis-like iterations between projection space and *xy* space. To compensate for the sparse coverage of projection space much smoothing was applied to fill the entire projection space, which unfortunately resulted in oversmoothing of the result. The improvements include taking into account the geometric properties of the imaging system [10] and the provision of a

sensible first approximation in the first iteration (instead of zero values). The first approximation is obtained by a CO method with an object function similar equation (16), with $\tilde{g}(p,\xi)$ replaced by $f(p,\xi)$ and with smallness on the edge imposed. This CO does not yield a consistent sinogram, but the inconsistency is adequately taken care of in the Gerchberg-Papoulis-like iterations of the IPR method.

4. PHANTOM SIMULATIONS

Phantom simulations, with the phantom of figures 1(a) and 3(a), were used to compare the CO-NBF method proposed in this paper with other tomography methods. The comparisons were done for the actual geometry of the JET soft x-ray imaging system. The other methods are: (A) the CO method on LBFs, which is the standard method used at JET; (B) an NBF method with TSVD and triangular-strip NBFs; (C) the improved IPR method described in section 3. Method A uses an advanced anisotropic unsmoothness object function that describes the expected emission very well [16]. Method B is the same as described in reference 22. However, in that application the number of basis functions was chosen similar to the number of measurements, whereas here for a fair comparison the same number of basis functions as in the other methods was used. The CO-NBF method has been applied with two types of NBFs: (D) the conventional triangular-strip NBFs and (E) the advanced NBFs that correspond to bi-linear interpolation in projection space (IPR like).

The quality of the reconstructions can be quantified in several ways. The first quantifier is the misfit between $\sigma_{\hat{f}}$ the backcalcuated values from the reconstruction and the measurements:

$$\sigma_{\hat{f}} = \frac{\left\| \boldsymbol{K}\boldsymbol{g} - \hat{\boldsymbol{f}} \right\|}{\left\| \hat{\boldsymbol{f}} \right\|} \tag{19}$$

where the bars indicate the Euclidean norm. The misfit indicates how well the reconstruction corresponds to measurements. Note that the misfit is equal to the constraint (17) (relatively), so that for the CO methods $\sigma_{\hat{f}}$ is an input parameter. For NBF methods, in equation (19) one can either use $\tilde{\boldsymbol{g}}$ and $\boldsymbol{K}$ from equation (13), or if the backprojection is expressed in LBFs, i.e. equation (12) is discretized for presentation purposes, $\boldsymbol{g}$ and $\boldsymbol{K}$ from equation (9); apart from discretization errors the misfit determined with both methods should be the same. When a phantom is available, more objective quantifiers for the reconstruction quality can be defined. If the subscript zero means phantom or derived from the phantom without any blurring by the geometric function, the tomogram error and sinogram error can be defined (if applicable) as

$$\sigma_g = \frac{\|g - g_0\|}{\|g_0\|} \text{ and } \sigma_f = \frac{\|f - f_0\|}{\|f_0\|}$$

respectively.

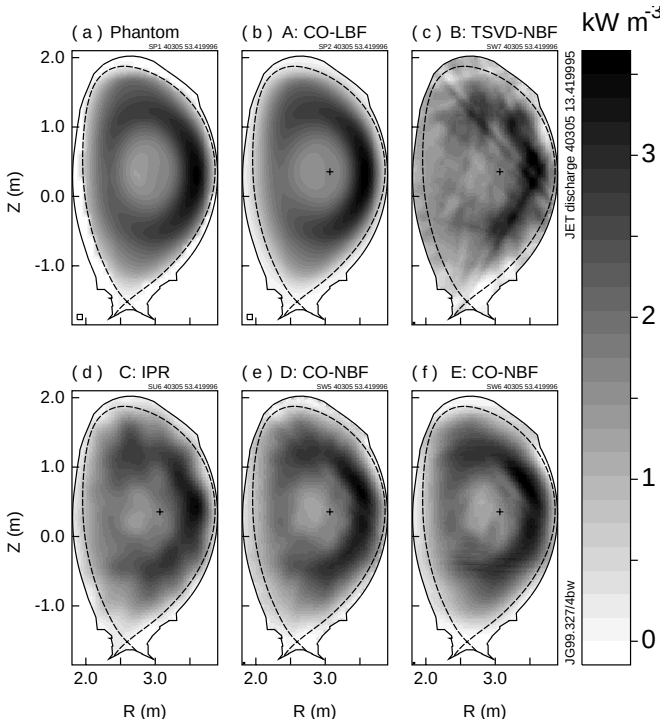

Fig.3: (a) Phantom soft x-ray emissivity. (b) Reconstruction with the standard CO on LBFs used at JET [16], method A. (c) Reconstruction with TSVD on triangular-strip NBFs [22], method B. (d) Reconstruction with IPR method, method C. (e) Reconstruction with CO on triangular-strip NBFs, method D. (f) Reconstruction with CO on IPR-like NBFs, method E. The square in the lower left corner indicates the grid size used to represent the data [in (b) this is the actual grid size of the reconstruction].

The phantom simulations were carried out with a realistic amount of noise: 3% relative Gaussian noise was added to the calculated measurements. The grid size was chosen to be able to represent the sinograms [fig.1(b)] and filtered sinograms [fig.2(a)] adequately, but not more than that to keep the computation time down. This required 51×16 $p\xi$ grid points [indicated in fig.2(d)]. The results are not very sensitive to the exact number if grid points (σ_g varied by less then 0.005 when the number of p or ξ points was increased or reduced by 3). The NBFs were implemented on a 100×200 xy grid, which is used for displaying and for calculating the tomogram error.

The intermediate results and reconstructions by the various methods are shown in figs.2 and 3. The NBFs were cut off at the reconstruction boundary indicated in fig.1. The optimum reconstruction errors obtained are summarized in table 1. In all cases the tomogram error was optimized by adjusting the reconstruction parameters: the truncation level in TSVD, the estimated error in CO, and various parameters in the IPR method. Note that the reconstructions cannot be optimized in this way when the phantom is not known, as is the case for actual measurements: in that case the experience from phantom simulations and the misfit have to be used to guess the most appropriate reconstruction parameters. In the case of CO the optimum reconstructions are obtained when the estimated errors are chosen smaller than the actual noise level; this is a well-known effect. Figure 2(a) shows the FBP-filtered sinogram of the phantom, i.e. the filtered sinogram that the solutions $\tilde{g}(p,\xi)$ of the regular-NBF methods can be compared with. The

Table 1: Reconstruction errors of the various reconstruction methods when applied to the phantom of figure 3(a). When applicable, the misfit $\sigma_{\hat{f}}$, tomogram error σ_g and sinogram error σ_f are given. The noise level in the simulations was 3%.

Reconstruction method	$\sigma_{\hat{f}}$	σ_g (%)	σ_f (%)
A: CO with LBF	2.5[a]	8.0	–
B: TSVD-NBF	1.8	25.9	–
C: IPR	3.6	14.7	5.4
D: CO-NBF (triangular strip)	1.9[a]	13.9	–
E: CO-NBF (IPR-like)	1.9[a]	12.3	–

[a] The misfit is an input parameter in these methods; there are some numerical variations between the input and output values.

NBF solutions for TSVD-NBF (method B) and CO-NBF with IPR-like basis functions (method E) are shown in figs.2(b) and 2(c), respectively. Because the scaling of the solution depends on the shape of the NBFs and the boundary region, only the shapes of these filtered sinograms and not the magnitudes are compared. It is clear that, thanks to the *a priori* information, the CO-NBF method achieves a result that is much closer to fig.2(a) than the TSVD-NBF method. Restoring the sinogram $f(p,\xi)$ from $\tilde{g}(p,\xi)$ by the projection-backprojection operator for line integrals, i.e. inverse FBP filtering [equation (22) using equation (21) from the appendix], fig.2(f), looks reasonably like the sinogram of fig.2(b) (note that, as discussed in the appendix, the projection-backprojection operator applied to the filtered sinogram can be made to approximate the sinogram arbitrarily close if the grid is sufficiently fine). The reconstructed sinogram [fig.2(e)] by the IPR method is also very reasonable (see sinogram error in table 1). Despite the IPR-sinogram being better than fig.2(f), the tomograms of the CO-NBF methods are closer to the phantom [fig.3 and table 1).

5. DISCUSSION AND CONCLUSIONS

The tomography methods proposed here perform significantly better than the TSVD-NBF method. The TSVD-NBF method with 51×16 NBFs is even not significantly better than TSVD with only 200 NBFs ($\sigma_g = 26.8\%$ [22]). The reason for the disappointing performance of the TSVD-NBF method is that, due to the irregular and incomplete coverage [see fig.1(b)], not enough information is available for a good reconstruction [20]. The CO methods with the irregular coverage, however, still perform significantly better than TSVD methods with more regular coverage with more views [22]. The non-TSVD methods all use smoothness as *a priori* information [for $g(x,y)$, $f(p,\xi)$ or $\tilde{g}(p,\xi)$], and some use smallness on the edge. The reason for the CO method with LBFs being best is probably that the object function for anisotropic smoothness has been particularly developed to describe the plasma emission in a tokamak well, whereas the anisotropic

smoothness in the other methods is *ad hoc*. More advanced object functions in projection space may well perform better. The CO-NBF methods perform slightly better than the IPR method, although the IPR method has a large number of parameters and it may be that there is a combination of parameters that is better for a given phantom than the parameters used in the present simulations. For some phantoms the IPR method is as good as the CO-NBF method with triangular-strip NBFs. It is surprising that that the IPR method does so well as the smoothness object function does not necessarily agree with the consistency conditions of projection space; in contrast, in CO-NBF the consistency conditions are automatically adhered to by the nature of the inversion. However, the IPR method can make use of the smallness-on-edge term in the object function, which turns out to be important. Finally, as predicted, the IPR-like NBFs are better than triangular-strip and constant-strip NBFs.

Considering the relationship between NBF methods and FBP leads to the application of constrained optimization to generalized NBF methods with smoothness as object function. The smoothness imposed on the expansion coefficients in projection space of NBF methods is equivalent to band-limiting in FBP. It has been shown that CO-NBF methods perform much better than conventional TSVD-NBF methods, in particular when the coverage of the imaging system is irregular. TSVD and CO are likely to be equally computationally intensive. The SVD does only need to be done once and the results stored, as long as the geometry and basis functions do not change; this means that once the SVD has been done, many reconstructions can be made in a very short time. The same is true for certain implementations of the CO method based on the generalized eigenvalue problem [19], as long as both the geometry and the object function do not change. A new type of NBF that describes bi-linear interpolation in projection space has been proposed, which gives better results than conventional NBFs. Also higher order interpolations can be used to define NBFs. A drawback of the new type of NBF is that it is very time-consuming to calculate; however, as long as the grid in projection space is not changed, the NBFs can be calculated once and stored. The new type of NBF was inspired by the type of projection-space basis function used in the IPR method. A new implementation of the IPR method was found to perform nearly as well as the CO-NBF method.

APPENDIX

This appendix discusses some relationships between filtered backprojection (FBP) and natural basis function (NBF) tomography methods. Both methods use a backprojection [equations (3) and (11)], which is equivalent if one considers the continuous form of FBP with line-integral basis functions $B(x,y \mid p,\xi) = \delta(p + x\sin\xi - y\cos\xi)$. The steps in FBP and continuous NBF to be compared are therefore equations (2) and (14). The continuous line-integral geometric function can be written as

$$K(p,\xi \mid x,y) = \delta(p + x\sin\xi - y\cos\xi)\,\Pi_{0,a^2}(x^2 + y^2). \tag{20}$$

The band-pass function Π in Eq. (20) is defined by

$$\Pi_{z_c,r}(z) = \begin{cases} 1 & \text{for } z_c - r < z < z_c + r \\ 0 & \text{otherwise} \end{cases}$$

and can be introduced without affecting the outcome of the Radon transform as g has finite support (i.e. is zero outside a circle with radius a). Substitution of $B(x,y \mid p,\xi)$ and $K(p,\xi \mid x,y)$ into equation (15) gives

$$\begin{aligned} &A(p,\xi \mid p',\xi') \\ &\quad = \int_{-\infty}^{\infty}\int_{-\infty}^{\infty} \delta(p + x\sin\xi - y\cos\xi)\,\delta(p' + x\sin\xi' - y\cos\xi')\,\Pi_{0,a^2}(x^2+y^2)\,\mathrm{d}x\,\mathrm{d}y\,. \end{aligned} \tag{21}$$

By inserting equation (3) into (1) and swapping the order of the integrals (which is allowed in all cases in this paper because the integrand is bounded), one can show that

$$f(p,\xi) = \int_0^{\pi}\int_{-\infty}^{\infty} h(p',\xi')\,A(p,\xi \mid p',\xi')\,\mathrm{d}p'\,\mathrm{d}\xi' \tag{22}$$

with the same $A(p,\xi \mid p',\xi')$ as in (21). Equations (22) and (14) are the same, thus $\tilde{g}(p,\xi)$ of equation (14) and $h(p,\xi)$ from equation (2) must be equivalent. Because equation (2) followed by (3) is equal to the inverse Radon transform, it must be the case that equation (22) is the inverse of (2). This means that continuous NBF and FBP are equivalent, but that the solution path is different: in an NBF method $\tilde{g}(p,\xi)$ has to be solved from equation (14), whereas in FBP an explicit expression exist for $\tilde{g}(p,\xi) = h(p,\xi)$ in the form of equation (2).

To give the final proof that FBP and NBF methods are equivalent, one has to show that, for example, Eq. (2) substituted into Eq. (22) leads to an equality. In the present work this equality has not been proven, nor has the author encountered such a proof in the literature. Numerical calculations, however, show that if one starts with a function $f(p,\xi)$ on a discrete grid, calculates $h(p,\xi)$ from Eq. (2) with a band-limited filter function, and substitutes this $h(p,\xi)$ for $\tilde{g}(p,\xi)$ into Eq. (22), one obtains a result very close to $f(p,\xi)$, increasingly so for finer and finer grids. In these numerical calculations the following explicit expressions for $A(p,\xi \mid p',\xi')$ were used. By integrating over the delta functions in Eq. (21) one can show that

$$A(p,\xi \mid p',\xi') = \frac{1}{\left|\sin(\xi - \xi')\right|}\,\Pi_{p'\cos(\xi-\xi'),\sin(\xi-\xi')\sqrt{a^2-p'^2}}(p).$$

In the singularity at $\xi = \xi'$ one can show that

$$\int_{-\infty}^{\infty} h(p',\xi)\,A(p,\xi \mid p',\xi)\,\mathrm{d}p' = 2\sqrt{a^2 - p^2}\,h(p,\xi).$$

The numerical calculations make it plausible that Eq. (22) is the inverse of Eq. (2). At first sight it may seem surprising that an equation with two integrals [Eq. (22)] is the inverse of an equation

with one integral [equation (2)]; cf. the inversion formula of the Radon transform. It seems likely that this is true only for functions $f(p,\xi)$ that are a Radon transform of an arbitrary function $g(x,y)$; i.e. the functions $f(p,\xi)$ have to satisfy the consistency conditions [1] of projection space. Indeed, similar numerical calculations as above show that with a function $f(p,\xi)$ that is not a valid Radon transform the result of Eq. (2) followed by Eq. (22) is very different from the original $f(p,\xi)$.

In practice NBF is not continuous and both basis functions and geometric functions are strips with finite width. So, one would expect NBF to give, at best, a blurred version of the FBP result. However, also the integrals of the FBP method have to be evaluated numerically with discrete data. In fact, using nearest neighbour or linear interpolation between samples in the evaluation of equation (2) is equivalent with the strip or triangular-strip NBFs given in figs.1(g) and 1(h). Also the regularization of the inversion of equation (13) will have an effect similar to the band-limitation of the filter function in equation (2). FBP has the drawback that it can only cope with regularly sampled data.

REFERENCES

[1] Lewitt R M 1983 "Reconstruction algorithms: transform methods" *Proc. IEEE* **71** 390–408

[2] Bracewell R N 1977 "Correction for collimator width (restoration) in reconstructive x-ray tomography" *J. Computer Assisted Tomography* **1** 6–15

[3] Lindgren A G and Rattey P A 1981 "The inverse discrete Radon transform with applications to tomographic imaging using projection data" *Advances in Electronics and Electron Physics* **56** 359–410

[4] Ogawa K, Paek S, Nakajima M, Yuta S, Kubo A and Hashimoto S 1988 "Correction of collimator aperture using a shift-variant deconvolution filter in gamma camera emission CT" in *Medical Imaging II*, Editors Schneider R H and Dwyer S J, Proc SPIE Vol. 914 699–706

[5] McCaughey D G and Andrews H C 1977 "Degrees of freedom for projection imaging" *IEEE Trans. Acoustics, Speech, Signal Processing* **ASSP-25** 63–73

[6] Verly J C 1982 "Collimator effects in high resolution x-ray computer tomography" *IEEE Trans. Med. Im.* **MI-1** 122–136

[7] Ingesson L C and Pickalov V V 1996 "An iterative projection-space reconstruction algorithm for tomography systems with irregular coverage" *J. Phys. D: Appl. Phys.* **29** 3009–3016

[8] Likhachov A V, Pickalov V V, Chugonova N V and Baranov V A 1999 "Development of iterative algorithms for industrial tomography" in *Proceedings of 1st World Congress on Industrial Process Tomography* (Mancheser, UK: VCIPT) 463–469

[9] Peters T M and Lewitt R M 1977 "Computed tomography with fan beam geometry" *J. Computer Assisted Tomography* **1** 429–436

[10] Ingesson L C, Böcker P J, Reichle R, Romanelli M and Smeulders M 1998 *Projection-space methods to take into account beam-width effects in two-dimensional tomography algorithms* Report JET-R(98)02 (Abingdon, UK: JET Joint Undertaking)
[11] Herman G T 1980 *Image reconstruction from projections* (New York: Academic Press)
[12] Buonocore M H, Brody W R and Macovski A 1981 "A natural pixel decomposition for two-dimensional image reconstruction" *IEEE Trans. Biomed. Eng.* **BME-28** 69–78
[13] Gullberg G T, Hsieh Y-L and Zeng G L 1996 "An SVD reconstruction algorithm using a natural pixel representation of the attenuated Radon transform" *IEEE Trans. Nucl. Sci.* **43** 295–303
[14] Baker J R, Budinger T F and Huesman R H 1992 "Generalized approach to inverse problems in tomography: image reconstruction for spatially variant systems using natural pixels" *Crit. Rev. Biomed. Eng.* **20** 47–71
[15] Hsieh Y-L, Gullberg G T, Zeng G L, Huesman R H 1996 "Image reconstruction using a generalized natural pixel basis" *IEEE Trans. Nucl. Sci.* **43** 2306–2319
[16] Ingesson L C, Alper B, Chen H, Edwards A W, Fehmers G C, Fuchs J C, Giannella R, Gill R D, Lauro-Taroni L and Romanelli M 1998 "Soft x-ray tomography during ELMs and impurity injection in JET" *Nucl. Fusion* **38** 1675–1694
[17] Ingesson L C, Böcker P J, Reichle R, Romanelli M and Smeulders P 1999 "Projection-space methods to take into account beam-width effects in two-dimensional tomography algorithms" *J. Opt. Soc. Am. A.* **16** 17–27
[18] Cormack A M 1964 "Representation of a function by its line integrals, with some radiological applications. II" *J. Appl. Phys.* **35** 2908–2913
[19] Fehmers G C, Kamp L P J and Sluijter F W 1998 "An algorithm for quadratic optimization with one quadratic constraint and one bounds on the variables" *Inverse Problems* **14** 893–901
[20] Hanson K M and Wecksung G W 1985 "Local basis-function approach to computed tomography" *Appl. Opt.* **24** 4028–4039
[21] Bertero M, Mol C de and Pike E R 1988 "Linear inverse problems with discrete data. II: Stability and regularisation" *Inverse Problems* **4** 573–594
[22] Ingesson L C, Chen H, Helander P, Mantsinen M J 2000 "Comparison of basis functions in soft X-ray tomography and observation of poloidal asymmetries in impurity density" *Plasma Phys. Control. Fusion* **42** 161–180